Research Square

Preprints are preliminary reports that have not undergone peer review.
They should not be considered conclusive, used to inform clinical practice,
or referenced by the media as validated information.

Demonstration of High Optical Conductivity, Thermoelectric Potential and Mechanical Stability of Newly Predicted Ruddlesden–Popper Cerates Compounds for Plasmonic and Optoelectronic Applications

Muhammad Ahsan

ahsan@qlit.edu.cn

Qilu Institute of Technology

Muhammad Ammar Yasir

Riphah International University

Rabia Zafar

University of the Punjab

Faisal Tufail

Riphah International University

Huda A. Alburaih

Princess Nourah bint Abdulrahman University

Sohail Mumtaz

Gachon University

Xie Fei

Qilu Institute of Technology

Research Article

Keywords: Layered perovskites, Ruddlesden–Popper phase, Rare earth cerates, DFT, Optoelectronics

Posted Date: September 14th, 2026

DOI: https://doi.org/10.21203/rs.3.rs-10694014/v1

License: This work is licensed under a Creative Commons Attribution 4.0 International License.
Read Full License

Additional Declarations: No competing interests reported.

Demonstration of High Optical Conductivity, Thermoelectric Potential and Mechanical Stability of Newly Predicted Ruddlesden–Popper Cerates Compounds for Plasmonic and Optoelectronic Applications

†Muhammad Ahsan*[1,] †Muhammad Ammar Yasir[2], Rabia Zafar[3], Faisal Tufail[2], Huda A. Alburaih[4], Sohail Mumtaz*[5], Xie Fei [1]

1. *Department of physics, Qilu institute of Technology, Jinan 250200, Shandong, China.*
2. *Department of Physics, RIPHAH International University, Campus Lahore, Pakistan*
3. *Centre of Excellence and Solid-State Physics, University of the Punjab, Lahore, 54770, Pakistan.*
4. *Department of Physics, College of Science, Princess Nourah Bint Abdulrahman University, P.O. Box 84428, Riyadh 11671, Saudi Arabia*
5. *Department of Chemical and Biological Engineering, Gachon University, 1342 Seongnamdaero, Sujeong-gu, Seongnam-si, 13120, Republic of Korea*

†Muhammad Ahsan and †Muhammad Ammar Yasir contributed equally in this study and share the 1st authorship status.

Corresponding Authors email: ahsan@qlit.edu.cn ; dr.ammarphysicist@gmail.com

Abstract

This study presents a theoretical investigation of the structural, mechanical, electronic, optical, thermodynamic, and plasmonic properties of the Ruddlesden–Popper phase X_2CeO_4 compounds (X = Mg, Sr, and Ba). The calculated electronic band structures indicate direct or indirect band gaps ranging from 1.9 to 2.3 eV, confirming the semiconductor nature of these materials and highlighting their significant potential for solar and optoelectronic applications. The optical analysis reveals the high optical conductivity (4500 to 6500 $\Omega^{-1}cm^{-1}$), the dielectric constant between 4 and 6, an absorption coefficient of around 10^5 cm^{-1}, and a refractive index of 2 to 2.5 in the visible to near-ultraviolet spectrum, supporting their usage in optoelectronic, photonic, and flexible electronic devices. The thermodynamic characteristics of X_2CeO_4 indicate enhanced

thermal stability above 900 K: as temperature increases, the materials expand in volume and increase in entropy, while their Gibbs Free Energy decreases, thereby improving thermal stability. Moreover, the Mg_2CeO_4 exhibits a somewhat elevated zT (0.9) at room temperature. This work highlights the multifunctional properties of X_2CeO_4 compounds and proposes their use in next-generation plasmonic, optoelectronic, and photovoltaic applications.

Keywords: Layered perovskites; Ruddlesden–Popper phase; Rare earth cerates; DFT; Optoelectronics

1. Introduction

In recent decades, technical breakthroughs in engineering operations and daily living have frequently been attended with an increase in environmental deterioration. In response to that urgent issue, intelligent energy structures along with renewable energy technologies have arisen as viable replacements, chiefly because of their capacity to substantially diminish destructive emissions throughout operation [1, 2]. Among the diverse renewable energy alternatives suggested to facilitate sustainable technological advancement, wind, geothermal, as well as tidal energy emerge as significant contributors [3, 4]. Light energy has gained significant importance, constituting the greatest proportion of executed renewable energy projects worldwide. In the field of solar innovations, photovoltaic (PV) technology has emerged as the greatest extensively utilized [5-7]. Their appeal arises from both their cost-effectiveness and their simplicity of installation, as well as their little maintenance needs. In the last thirty years, photovoltaic technology has experienced significant advancements in its technological capabilities and applications [8-10]. Photovoltaic technology has a unique characteristic that differentiates it from alternative renewable sources of energy sources and solar-centric systems specifically [11]. Although several renewable resources

are increasingly integrated into the worldwide energy framework, their efficiency is mostly constrained by the attributes of the source rather than the application domain [12]. Conversely, PV classifications operate as application-specific energy sources, providing enhanced versatility as well as integration possibilities across multiple sectors [13]. Historically, photovoltaic technology has been utilized in aircraft missions to energize satellites and is currently being investigated for airline propulsion systems. This degree of adaptability is rarely observed in additional renewable sources like geothermal, wind, and wave energy, which are constrained by environmental along with locational factors [14]. Oxide-based luminous materials have been extensively investigated owing to their inherent qualities, which are often modified by altering compositions for appropriate substitutes or by uniquely integrating desirable characteristics [15]. Danielson *et al.* discovered that a novel oxide-based blue phosphor (Sr_2CeO_4) demonstrates blue-white illumination attributed to the charge transfer (CT) process [16]. As a significant member of oxide-based luminescent materials, Sr_2CeO_4 is an effective photoluminescent material [17, 18], making it suitable for the production of optoelectronic devices, including blue-emitting lamp phosphors, photoluminescent as well as electroluminescent devices. Strontium cerium oxide (Sr_2CeO_4) is a member of the RPP family of layered perovskite materials, defined by the generic chemical formula $A_{n+1}B_nO_{3n+1}$. In this formula, A generally signifies alkaline earth metals, B indicates transition metals, along with n is an integer (n = 1, 2, 3, …). The materials in this course are recognized for their many uses in energy storage along with conversion technologies. Notably, Sr_2CeO_4 has demonstrated promising properties as a solid electrolytes in solid-state fuel cell cells (SOFCs), which efficiently transform chemical energy into electrical energy [19]. Beyond electrochemical purposes, RPP compounds display considerable optical characteristics, making them appropriate for use in laser devices, optical waveguides, along with photodetectors [20]. Talik et al. discovered that Sr_2CeO_4 acts as a

luminous material, exhibiting charge-transfer (CT) illumination of Ce^{4+} ions when activated by ultraviolet (UV) radiation at ambient temperature [21]. Additionally, photoluminescence response of Sr_2CeO_4 was investigated by Danielson *et. al,* revealing an energy transfer process between O^{2-} and Ce^{4+} ions inside one-dimensional chains produced by edge-sharing CeO_6 octahedra [16]. Undoped Sr_2CeO_4 is a promising blue-emitting phosphor with great thermal as well as chemical stability and outstanding optical characteristics [22]. Despite these discoveries, the extant literature has limited, extensive research on the physical characteristics of these molecules. Therefore, it was considered worthwhile to predict cation exchange X_2CeO_4 Under identical settings, compare the structural, electrical, along with optical properties. Here in the current manuscript, we studied the X_2CeO_4 (X = Mg, Sr, Ba) Compounds using a DFT approach, and the derived values of electronic characteristics such as bandgaps provided insight into their nature, allowing their use in PV and optoelectronic applications. Furthermore, spectral region-dependent optical properties such as dielectric function, reflectivity, refractive index, absorption, loss function, as well as optical conductivity have been estimated for these materials. Furthermore, thermodynamic aspects are studied, which are fundamental needs for optoelectronic applications.

2. Computational methodology

The most extensively utilized first principal approach was used to explore a variety of physical properties, including structural and electronic (density of states, band-structure), thermodynamic, and the optical analysis include real and imaginary dielectric functions, reflectivity, refractive index, absorption, extinction coefficient, optical conductivity, along with loss function. The WIEN2K [23] code was used to apply Perdew Burke Ernzerhof (PBE-sol) exchange-correlation-function, the periodic condition, and Generalized-Gradient-Approximation (GGA) of DFT computations [24] utilizing the mBJ [25] potential to precisely determine the electronic

structure. Optimized parameters obtained from geometry optimization of the unit cell with Murnaghan Equation of state fitting [26] and forces minimization were used to calculate the SCF for density of states (DOS), band structure, and optical properties. KPOINTS convergence [27] was achieved using a 2000-point K-mesh (12 × 12 × 12); To make sure accuracy, the k-point mesh used in the electronic band structure calculations was enhanced as $20 \times 20 \times 20$ with denser measurement at high symmetry points. To ensure that precision, parameters such as RMT × K_{max} (K-vector), (muffin-tin radius) = 7, Gmax (Gaussian factor) = 18, and l_{max} (angular momentum vector) = 10 were rigorously chosen based on estimated values that converged on 10^{-4} Ry [28]. We have also calculated the formation energy E_f of the studied compounds as reported earlier [29-31]

3. Results and discussion

3.1 Crystal structure and stability

Fig. 1 depicts the orthorhombic crystal structure of X_2CeO_4 materials, with X representing Mg, Sr, and Ba, computed by the Pbam space group and consisting of 14 atoms per unit cell. The structural model utilized for this investigation aligns with the optimum structure of mp-15743. The unit cell model of the crystal is also illustrated in Fig.1 for enhanced visualization. The optimized lattice constants for each variation of X_2CeO_4 exhibiting orthorhombic symmetry are presented in Table 1.

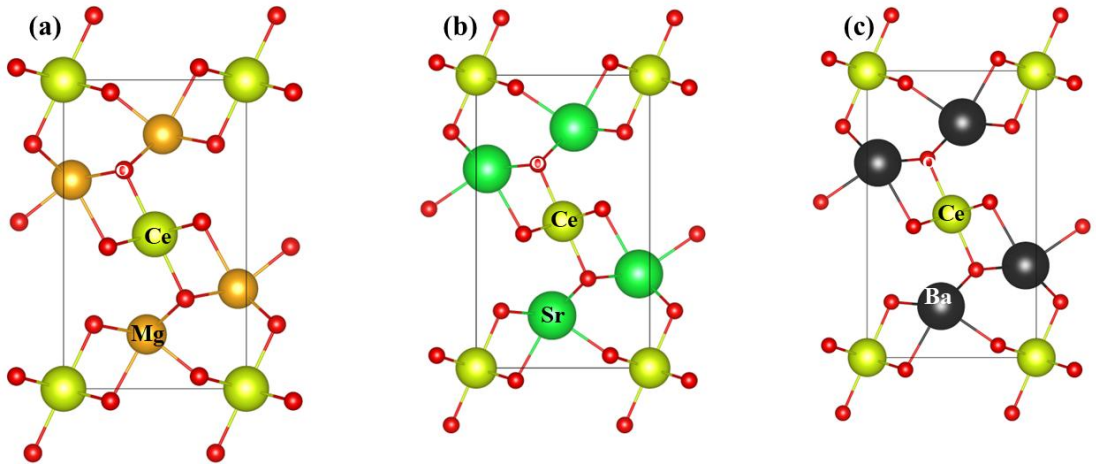


Fig.1. Unit cell crystal structure of X_2CeO_4 (X = Mg, Sr, Ba) compounds.

Table 1 demonstrates that the crystal structure undergoes a gradual expansion with the incorporation of various tetravalent atoms, adhering to the following sequence: Ba_2CeO_4 > Sr_2CeO_4 > Mg_2CeO_4. This variation is mostly ascribed to the discrepancies in the ionic radii of the replaced tetravalent cations [32]. Magnesium (Mg^{2+}) has the shortest ionic radius 72pm, while barium (Ba^{2+}) has a comparatively greater ionic radius 135pm. Accordingly, the Ba_2CeO_4 material demonstrates the greatest lattice parameters, while the Sr_2CeO_4 and Mg_2CeO_4 compounds exhibit considerably lesser values, confirming the observed structural trend. The Fig. 2 represents the energy versus volume optimization curves of the ternary cerates of Mg_2CeO_4, Sr_2CeO_4, and Ba_2CeO_4 with the intention of determining the stable equilibrium states. The minima of the curve of each of the parabolic curves can be used (by equating the calculated energy points to an equation of state) to define the equilibrium unit cell volume at which the material should be in its most energy-stable state [33]. The equilibrium volume of the solution of the Ba_2CeO_4 Fig.(c) is far more in the order of 1740 $(a.u)^3$ compared to that of Mg_2 CeO_4, Sr_2CeO_4, Fig(a-b) at about 1320 $(a.u)^3$ which is directly related to the higher ionic radius of Barium compared to Magnesium.

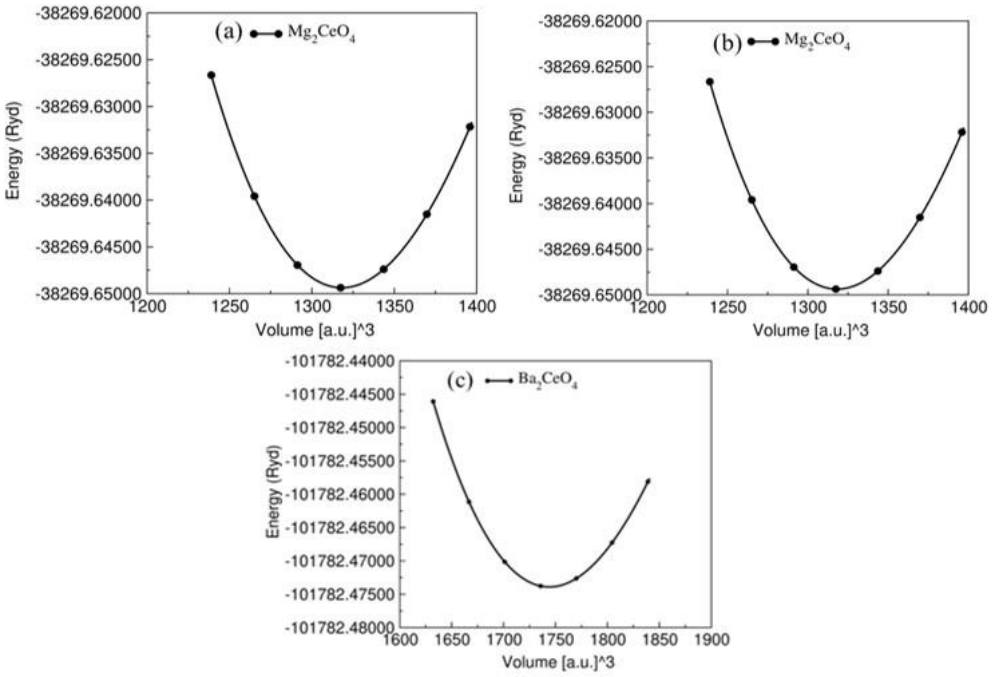


Fig.2. The volume optimization plot of (a) Mg_2CeO_4, (b) Sr_2CeO_4, and (c) Ba_2CeO_4

Table 1. Optimized lattice parameters and lattice constants of X_2CeO_4 (X = Mg, Sr, Ba) compounds

Materials	**a (Å)**	**b (Å)**	**c (Å)**	**α/β/γ**	**Band gap**	E_f	**Ref**
Mg_2CeO_4	5.80	9.80	3.43	90	1.9 eV	-4.51	This work
Sr_2CeO_4	6.12	10.34	3.61	90	2.3 eV	-4.99	[34, 35]
Ba_2CeO_4	6.36	10.76	3.76	90	2.0 eV	-4.83	This work

The mechanical behavior and elastic constants of these Ruddlesden–Popper cerate compounds were computed using the first principles calculations. The elastic constants (second order) are derived from the application of a small strain. The mechanical stability conditions under the Born stability criteria for orthorhombic crystals C_{11}, C_{22}, $C_{33} > 0$, C_{44}, C_{55}, $C_{66} > 0$, $C_{11} + C_{22} - 2C_{12} > 0$, $C_{11} + C_{33} - 2C_{13} > 0$, and $C_{22} + C_{33} - 2C_{23} > 0$ are satisfied for all the three configurations. The Cij parameters of X_2CeO_4, (X = Mg, Sr, Ba) are listed below in table 2.

Table 2. The Cij parameters and some mechanical aspects of X_2CeO_4, (X = Mg, Sr, Ba).

Compounds	**C_{11}**	**C_{22}**	**C_{33}**	**C_{12}**	**C_{13}**	**C_{23}**	**C_{44}**	**C_{55}**	**C_{66}**
Mg_2CeO_4	174.953	205.597	240.139	64.298	65.279	95.059	67.665	16.974	31.155
Sr_2CeO_4	194.089	128.927	206.630	68.998	59.078	80.543	59.497	35.199	48.530

Ba_2CeO_4	168.804	116.890	174.671	84.393	62.861	74.817	49.266	30.975	42.404

Bulk modulus, Shear modulus, Young's modulus and Poisson ratio were calculated using Voigt approximations given as;

$$B = \frac{1}{9}\left(C_{11} + C_{12} + C_{33} + 2(C_{12} + C_{13} + C_{23})\right) \quad (1)$$

$$G = \frac{1}{15}\left(C_{11} + C_{12} + C_{33} - (C_{12} + C_{13} + C_{23}) + 3(C_{44} + C_{55} + C_{66})\right) \quad (2)$$

$$E = \frac{9BG}{3B + G} \quad (3)$$

And

$$v = \frac{3B - 2G}{2(3B + G)} \quad (4)$$

The evaluated values of elastic moduli are listed in table 3.

Table 3. The calculated elastic moduli of X_2CeO_4, (X = Mg, Sr, Ba) using Voigt approximation.

Mechanical Parameters	**Mg_2CeO_4**	**Sr_2CeO_4**	**Ba_2CeO_4**
Bulk modulus (B)	134.3	105.2	105.6
Shear modulus (G)	71.6	50.0	47.5
Young's modulus (E)	178.5	128.5	123.2
Poisson ratio (v)	0.247	0.295	0.299
Anisotropy index (A^U)	2.85	1.70	1.53

The B exceeded G in all the cases, indicating the compounds under investigation exhibit greater resistance to volumetric deformation compared to shape deformation. However, it is noted that Mg_2CeO_4 exhibits the highest elastic moduli ratios referring it as the stiffest compositions among the three owing to its smallest ionic radius. The anisotropic index also suggests a gradual transition from highly anisotropic to relatively isotropic trend as we substitute the A-site cation from Mg → Sr → Ba. The Poisson's ratio further validates this trend indicating a transition towards more ductility (B/G > 1.75) with increasing A-site cation radius. These mechanical trends can be directly corelated to the structural characteristics i.e smaller the cation radius leads to the higher stiffness due to shorter bond lengths.

Figure 3 shows the three-dimensional plots of linear compressibility, Poisson ratio, shear modulus, and Young's modulus of ELATE analysis to completely analyze the anisotropy of elasticity of

Mg_2CeO_4, Sr_2CeO_4, and Ba_2CeO_4. The fact that these surfaces are not perfectly symmetrical in terms of their spherical symmetry is used to show how much the elastic response is directionally dependent. The linear compressibility surfaces in figure 3 (a) indicate that the Mg_2CeO_4 is usually ellipsoidal in shape with symmetry. This implies that it is capable of tackling hydrostatic compression of all angles. On the other hand, the geometries of Sr_2CeO_4, and Ba_2CeO_4 (figure 3b and 3c) are increasingly deformed with substantial extension along some crystallographic axes. This implies that they are anisotropic and soft in certain directions. This graph indicates that compressibility anisotropy gradually increases with the progression of Mg_2CeO_4 to Ba_2CeO_4. The A-site cation has an ionic radius that increases the size of the lattice and weakens the bond strength. This is consistent with other earlier research on the perovskite-related materials [36, 37]. This trend is supported by the Poisson ratio. The margins of Mg_2CeO_4 are even and smooth, indicating that the elastic properties of Mg_2CeO_4 are stable, and somewhat anisotropic. Conversely, the shape of Sr_2CeO_4, and Ba_2CeO_4 is not regular. The shear modulus surfaces suggest that Mg_2CeO_4 has a relatively compact and less deformed geometry, which is associated with increased isotropic resistance to shear deformation. On the other hand, Sr_2CeO_4, and Ba_2CeO_4 exhibit significant distortions of certain soft and hard orientations, highlighting increased elastic heterogeneity and reduced shear resistance of specific planes. The Young's modulus surfaces offer additional understanding of the directional stiffness of these materials. The distribution of Mg_2CeO_4 is highly anisotropic with a strong sense of elongation implying strong rigidity along some directions and relative softness in others. Conversely, Sr_2CeO_4 is more heterogeneous in its stiffness profile compared to Ba_2CeO_4 which has a more homogeneous, albeit smaller, surface suggesting an overall decrease in stiffness. The observed reduction in stiffness of Mg_2CeO_4 to Ba_2CeO_4 is associated with the increase in lattice parameters and weakening of the interatomic interaction of larger A-site cations.

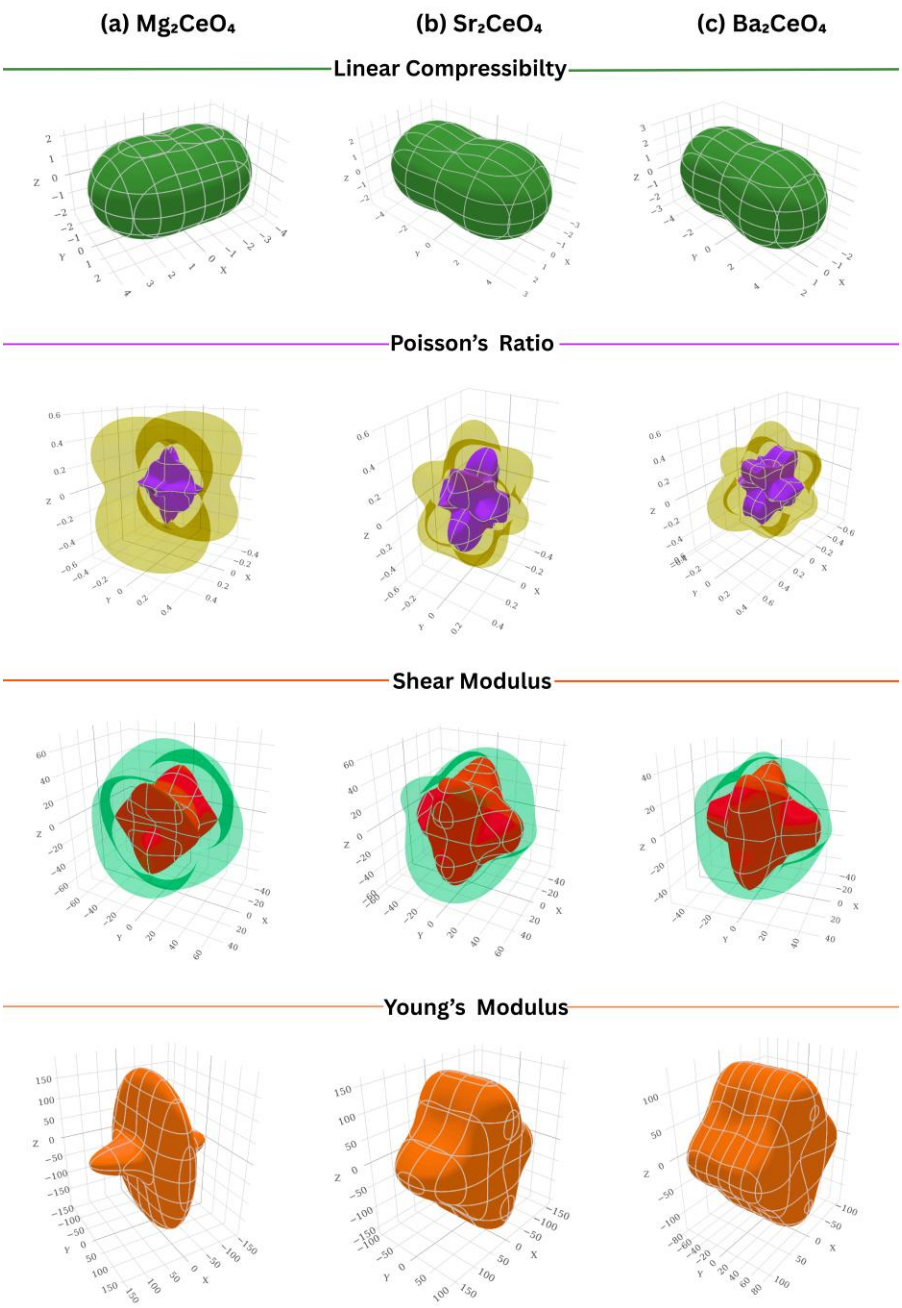


Fig 3. 2D and 3D representations of spatial dimensions parameters of X_2CeO_4 (X = Mg, Sr, Ba).

Such findings reveal that elastic anisotropy continues to rise in a systematic fashion with cation size, but mechanical stiffness decreases, which highlight the substantial effects of ionic substitution on the mechanical characteristics of such compounds in possible applications in optoelectronic

and structural devices. These findings are further supported by known anisotropy measures, such as the universal anisotropy index and the Voigt-Reuss-Hill approximations [4-6].

The phonon dispersion relations for orthorhombic X_2CeO_4 (where X = Mg, Sr, and Ba) materials were computed at high-symmetry locations in the Brillouin zone across a frequency spectrum of 0 to 20 THz, as illustrated in Fig. 4(a–c). The derived phonon band spectra along the high symmetry directions (Γ–X–S–Y–U–R–Z) of the Brillouin zone demonstrates the absence of imaginary frequencies at the gamma-point, demonstrating the dynamic stability of the compounds [38], as depicted in Fig. 4(a–c). The slight differences in the phonon branching among the compounds are due to differences in atomic mass and bond strength, and are seen to be smaller for the heavier alkaline-earth elements. The calculated phonon spectra show that these orthorhombic cerates are structurally stable and have a favorable lattice dynamic.

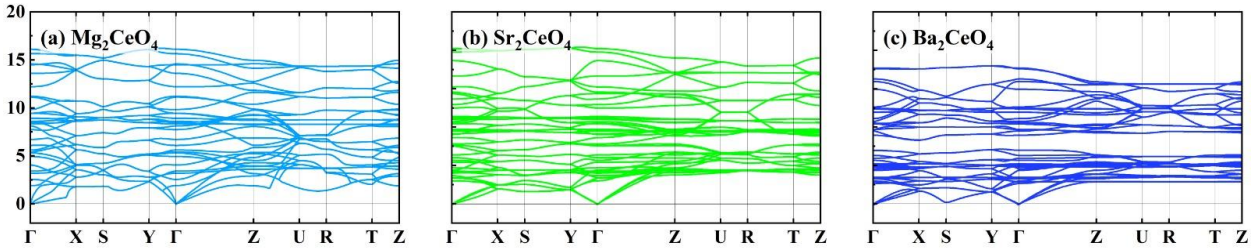


Fig 4. The computed Phonon spectra for X_2CeO_4 (X = Mg, Sr, Ba).

Furthermore ab-initio molecular dynamic simulations are shown below in figure 5, to ascertain the thermodynamic stability of X_2CeO_4 (X = Mg, Sr, Ba), we conducted the ab-initio molecular dynamic simulations [30] from the total energy profiles of Mg_2CeO_4, Sr_2CeO_4, and Ba_2CeO_4, and the total energy changes over the time interval of 5 ps, confirms the three compounds are thermally stable demonstrated in figures 5(a), 5(b) and 5(c) respectively. The cumulative energy fluctuates around -95.5 eV for Mg_2CeO_4 (approximately -96.0 to -94.9 eV), -101.1 eV for Sr_2CeO_4 (around -101.25 to -100.95 eV), and -100.2 eV for Ba_2CeO_4 (about -100.55 to -99.95 eV) with no significant energy variation. They are caused by small temperature fluctuations and atomic motions that occur at a non-zero temperature, and not by breaking or changing the structure. The crystal lattices are found to be preserved throughout the simulation and hence the average energy values are seen to be stable throughout in all the three orthorhombic cerates, which exhibits the thermal stability and durability of all the three orthorhombic cerates.

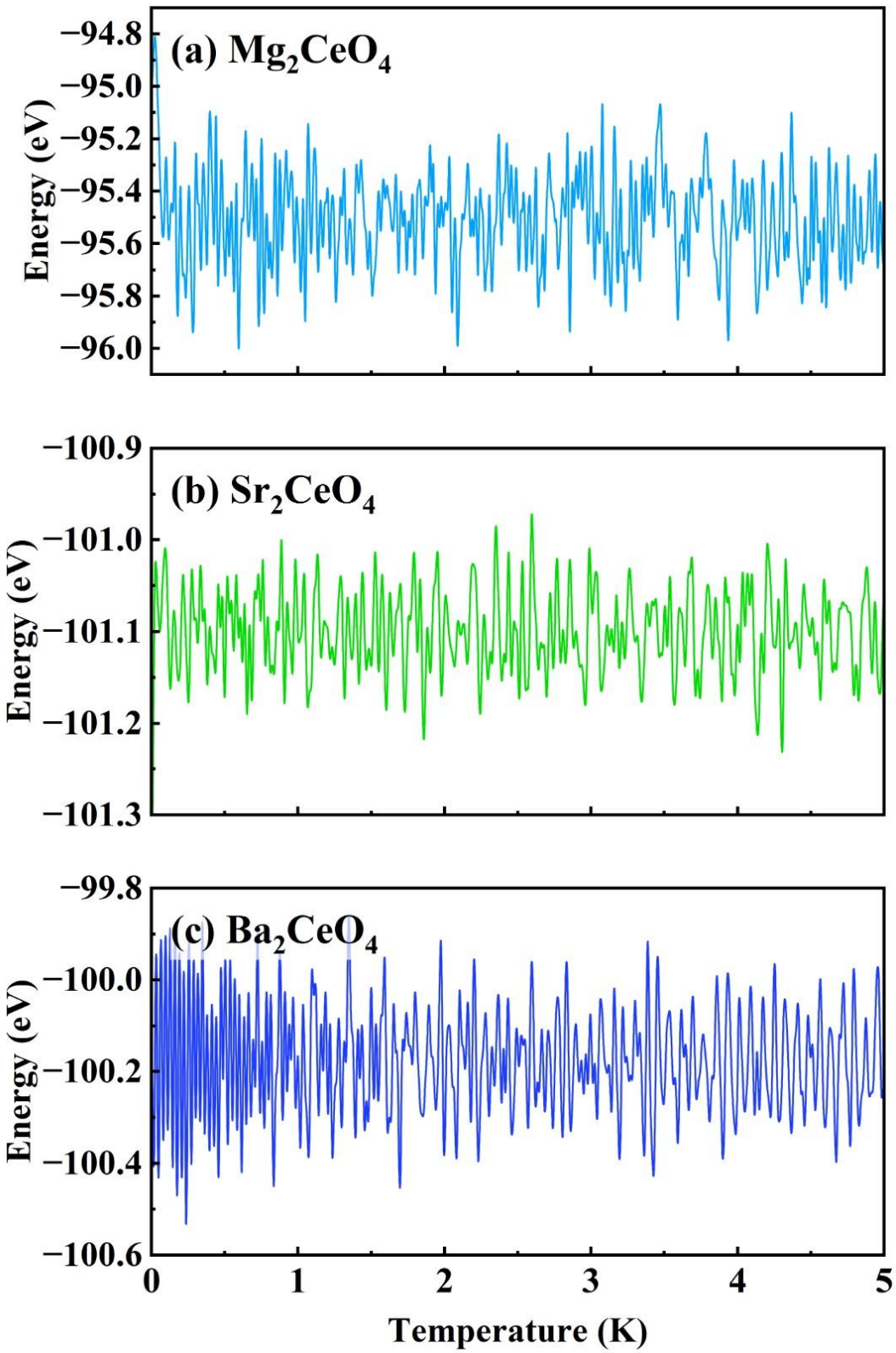


Fig 5. The AIMD simulation for X_2CeO_4 (X = Mg, Sr, Ba).

3.2 Electronic structure analysis

The bandgaps calculated using both the PBE along with TB-mBJ functional techniques are presented in Table 1. The TB-mBJ functional provided more accurate computed bandgap energies in comparison to experimental and theoretical values than those derived via PBE [34, 35, 39].

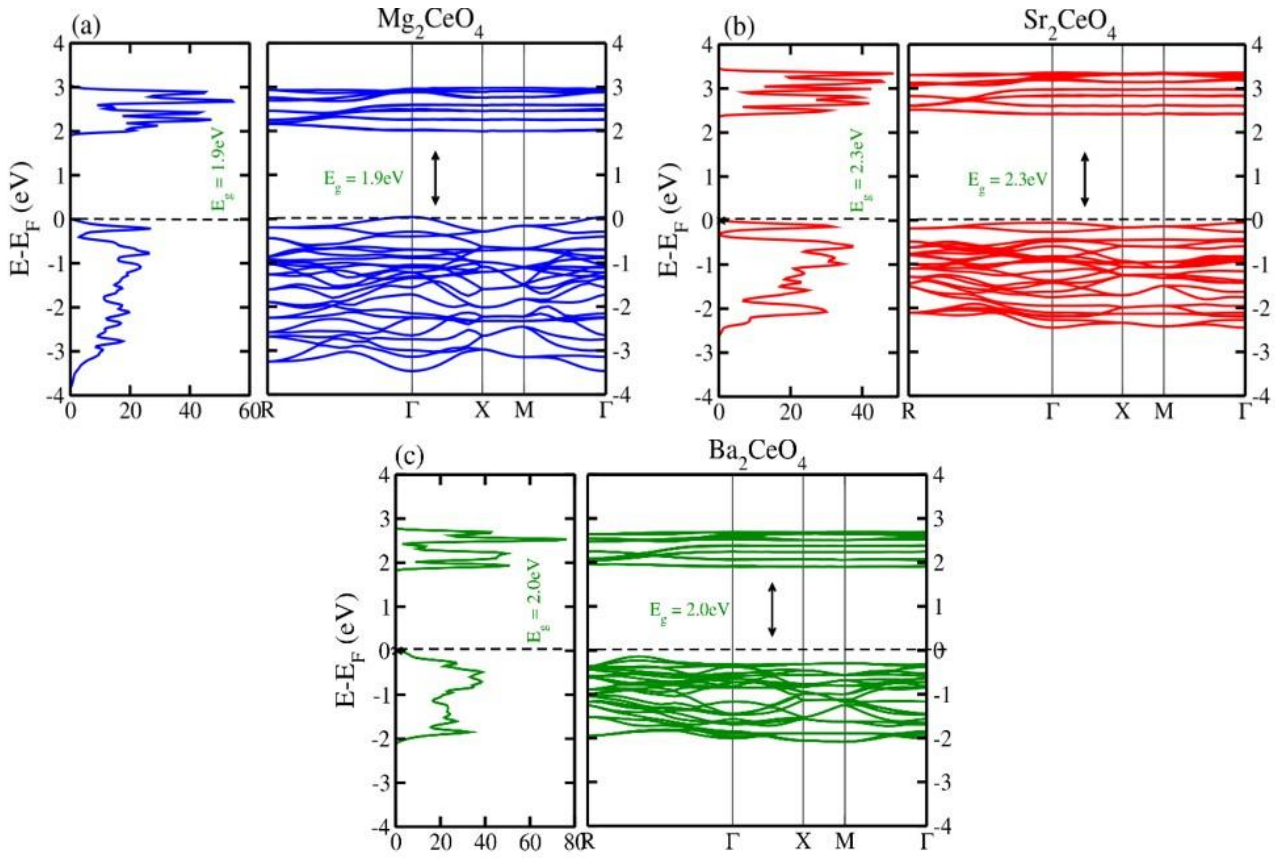


Fig 6. The electronic band structures and total DOS for X_2CeO_4 (X = Mg, Sr, Ba)

To obtain a deeper understanding of the electronic properties of the material X_2CeO_4 (X = Mg, Sr, Ba), we examined the electronic band structure as well as density of states (states/eV). The total density of states (DOS) along with band structure of X_2CeO_4 (X = Mg, Sr, Ba) were shown in Fig. 6. The energy range for the band structure along with total density of states (TDOS) graphs is from 4 eV to -4 eV. In the energy band configuration separation, the dashed line denotes the Fermi level or zero line in both Figures [40]. The electrical band structures of X_2CeO_4 (X = Mg, Sr, Ba) compounds are evaluated along high symmetry lines, as illustrated in Fig. 6. The Fig. 6 illustrates the band structures with band gaps of 1.9 eV, 2.3 eV, and 2.0 eV for the X_2CeO_4 (X = Mg, Sr, Ba)

compounds, computed using the GGA+mBJ method. The main component of the valence band is the O-2p states, and the main component of conduction band is the Ce-4f/5d states, which indicates that the O-2p states to the Ce-d/f orbital hybridization are the key electronic transitions. Alkaline-earth cation (Mg, Sr, Ba) changes cause substantial changes in band dispersion and density of states properties, which characterizes changes in the lattice parameters and conditions of bonding. The obtained effects allow concluding that electronic structure of X_2CeO_4 can be adjusted using appropriate cation substitution. The computed band structures of the materials illustrate the electronic transitions among the valence as well as conduction bands along high-symmetry trajectories in the involved Brillouin zone (IBZ), offering insights into the electrical characteristics of materials [41]. Each compound exhibits conduction band minima along with valence band maxima between the high-symmetry points T and X, indicating that the compounds possess either direct or indirect band structures [42]. The emergence of distinct peaks in the absorption bands is signified by electronic transitions among the valence band and conduction band sub-energy levels [43]. An indirect electronic band gap transition happens when the high-symmetry positions of the valence band maximum (VBM) as well as conduction band minimum (CBM) diverge; conversely, a direct electronic band gap transition occurs when these positions coincide [44]. Fig. 4(c) illustrates that the Ba_2CeO_4 compound has an indirect band structure, whereas band structures of Mg_2CeO_4, and Sr_2CeO_4, compounds are direct. The band gaps of these materials indicate their suitability for optoelectronic devices. The quantity of distinct energy states inhabited by electrons at a specific energy level is referred to as the Total Density of States (TDOS), representing the number of electronic states per unit volume per unit energy [45]. This function delineates fundamental properties of conductive compounds, paramagnetic susceptibility, encompassing specific heat, and many transport phenomena [46]. The TDOS simulations along with the total delivery state as a function of energy can be utilized to determine the energy band arrangement in semiconductors. Fig. 6 illustrates the electronic placement of the energy spectrum for each material as a function of the total density of states (TDOS) data.

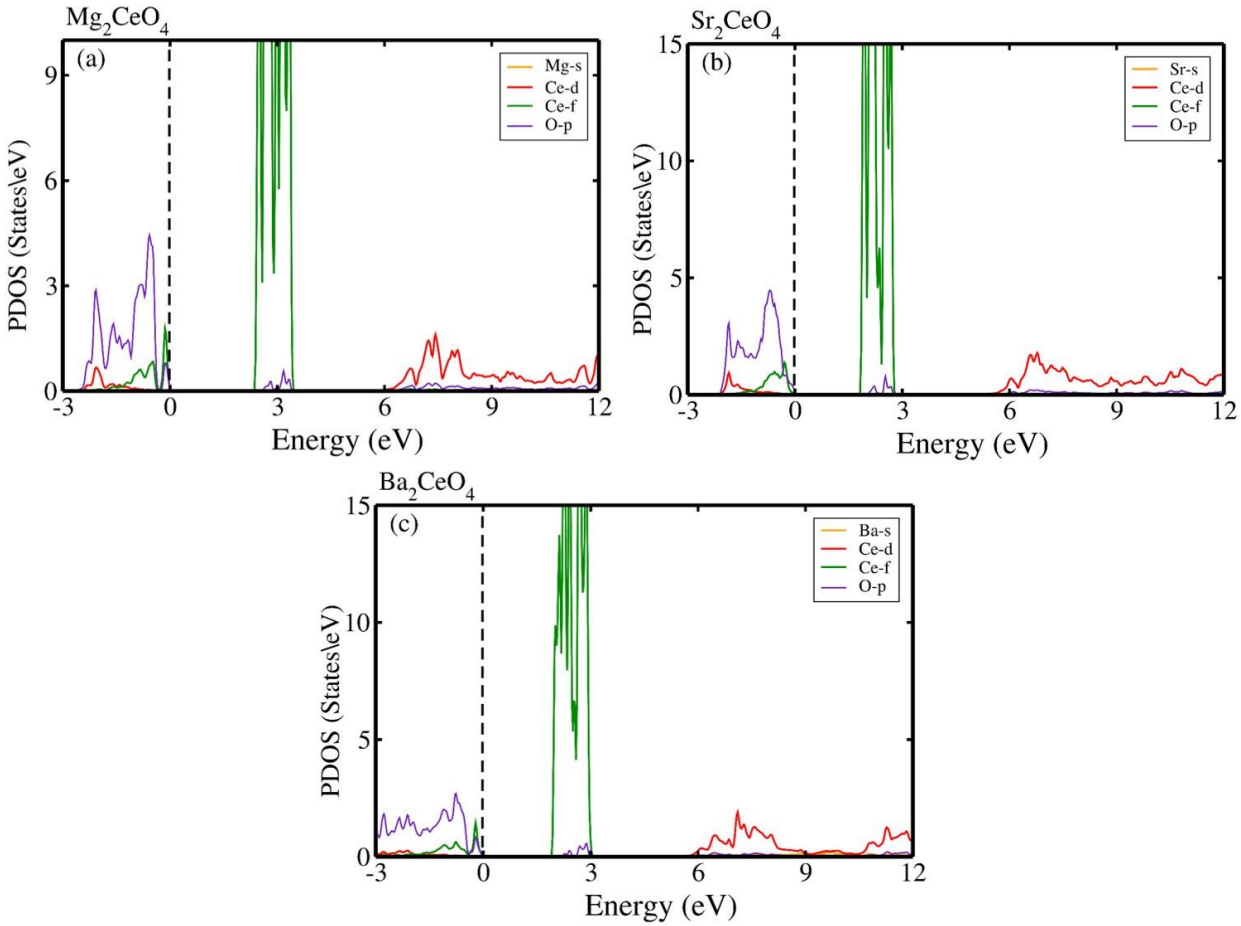


Figure 7: PDOS of (a) Mg_2CeO_4, (b) Sr_2CeO_4, and (c) Ba_2CeO_4

The PDOS of Mg_2CeO_4 shows that the valence band (-3 to 0 eV) is mainly composed of O-2p states with a maximum around 4.3 states/eV near the region of −0.5 eV. The Ce-4f states barely interact with the occupied part of the band and are tightly confined in the conduction band between 2.7 and 3.5 eV, where there are clear peaks with around 10 states/eV. At high energy levels (6-12 eV) the Ce-5d levels dominate with wide peaks at 1.5-1.7 states/eV. The lack of states at the Fermi level substantiates the semiconducting characteristics of Mg_2CeO_4, but the Mg-s orbitals have a minimal impact on the electronic configuration.

In figure 7b the O-2p orbitals play the major role in the valence band of Sr_2CeO_4, showing peak (about 4.4 states/eV) at about −0.4 eV. The absence of any states at the Fermi energy confirms the semiconducting properties. The Ce-4f peaks are also very prominent in the conduction band of the energy range 1.8 to 2.8 eV, reaching almost above15 states/eV, indicating more localization in the conduction band than in Mg_2CeO_4. The conduction band between 6 and 12 eV is largely made up

of the Ce-5d states, while the contribution from the Sr-s orbitals is small throughout the energy range.

The valence band of the PDOS of Ba_2CeO_4 is shown to be mainly composed of O-2p states, although the peak intensity of these states (at about 2.5–2.7 states/eV) is lower than that of Mg_2CeO_4 and Sr_2CeO_4. Like the other substances, there are no electronic states at the Fermi level, which indicates semiconducting properties. The Ce-5d states are present in the higher energy conduction region (6-12 eV) showing more widespread characteristics while Ce-4f states dominate the lower conduction band (2-3 eV) with well-defined peaks of ~15 states/eV. Also, the contribution is small in the Ba-s states, suggesting that the electrical properties depend mainly on the Ce and O orbitals.

The electronic configuration of these compounds is mainly determined by the Ce–O interaction, while the change of A-site cation slightly changes the strength and position of the electronic states while keeping the semiconducting properties unchanged.

3.3 Optical response and dielectric function

The optical response of X_2CeO_4 compounds is characterized by the frequency- dependent complex dielectric function, $\varepsilon(\omega) = \varepsilon_1(\omega) + i\varepsilon_2(\omega)$, as illustrated in Fig. 8. The real part of the dielectric constant $\varepsilon_1(\omega)$, determines the polarization and dispersive attributes of these materials X_2CeO_4 (X = Mg, Sr, Ba). In Fig. 8(a), it can be seen that all three compounds show a rapid increase in the value of epsilon $\varepsilon_1(\omega)$ at low wavelengths followed by a multiplicity of significant peaks, which are an indication of electronic transitions in the crystal lattice [47]. Ba_2CeO_4 (green line), has a peak of roughly 5.2 at about 180nm while Sr_2CeO_4 (red line), shows a peak of about 5.0 at about 150nm. It is significant to note that the peak of Mg_2CeO_4 (bluish line) has a much broader peak, with the peak at a higher value of around 5.1 at a much higher wavelength of about 450 nm. The high scores in the visible spectrum show that such materials have a strong ability to store electromagnetic energy which makes them suitable in optical applications. The imaginary term, which is the absorption of energy, and the beginning of electronic excitation is specified by the imaginary term, the epsilon $\varepsilon_2(\omega)$ [48]. Fig. 8(b) indicates that the highest energy peaks in the absorption spectrum were observed at the deep UV region, most probably caused by the transfer of charge between the oxygen atom and the cerium atom. The Fig. 8(b) of Ba_2CeO_4 presented the strongest absorption, having a major absorption peak of approximately 5.5 and a minor absorption

peak of 3.0. On the other hand, the absorption pattern of 2.7 is deep and at 300 nm with Sr_2CeO_4 2.7 but in the case of Mg_2CeO_4 2.6 it is at 350 nm. The gradual shifting of these peaks to longer wavelengths as the cation size increases, i.e. Magnesium to Barium, indicates a direct modulation of the electronic bandgap which is a major property of these layered materials.

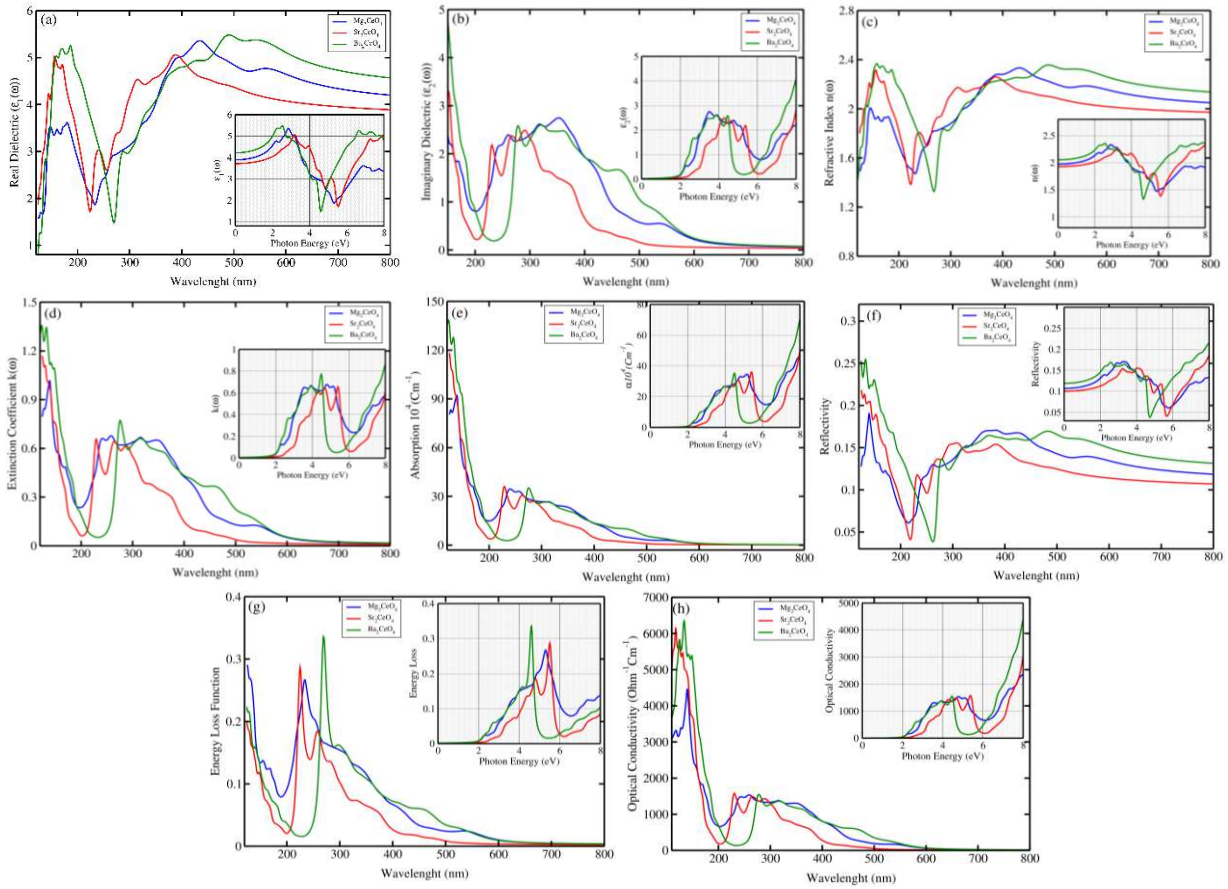


Fig 8. The calculated (a) real part $\varepsilon_1(\omega)$, (b) imaginary part $\varepsilon_2(\omega)$, (c) refractive index $n(\omega)$, (d) the extinction co-efficient $k(\omega)$, (e) Optical Conductivity $\sigma(\omega)$, (f) Absorption Coefficient $\alpha(\omega)$, (g) reflectivity $R(\omega)$, and (h) Loss Function $L(\omega)$ for X_2CeO_4 (X = Mg, Sr, Ba)

The refractive index, $n(\omega)$ describes the phase velocity of light passing through a compound and is closely related to the real part of dielectric function [49]. Fig. 8(c) represents that the refractive index of the three compounds, Mg_2CeO_4, Sr_2CeO_4, and Ba_2CeO_4 has a significant change in the ultraviolet region before stabilizing in the visible region. Ba_2CeO_4 (green line) has a dominating peak at 2.4 at around 150 nm and also a peak at 2.2 at 450 nm, whereas Sr_2CeO_4 (red line) has a peak value High values of the quantity $n(\omega)$ in the spectrum of visible light (between 1.8 and 2.2)

define that these materials are efficient in refracting and confining light, which is an important requirement in high-efficiency phosphors. The extinction coefficient, k(ω) represents the loss of energy that is due to absorption as light travels through the material [50]. Fig. 8(d) shows that the values of k(ω) are highest at the ultraviolet regime confirming that the materials are strong UV absorbers and A secondary peak of 0.8 in the wavelength of about 280 nm. Ba_2CeO_4, Mg_2CeO_4, has a broader absorption spectrum with a peak of 0.7 at approximately 320 nm. The rapid decrease in the values of k(ω) of the material towards the visible spectrum (at wavelengths longer than 500 nm) confirms that these materials become transparent to the visible light waves, allowing the blue-white light to escape the crystal without refreezing. The absorption coefficient is denoted by α(ω), and it is the ability of some materials to absorb incident photons of a certain energy [51]. Fig. 8(e) indicates that all three compounds show a strong absorption in the ultraviolet region, i.e., denotes a charge transfer transition between the oxygen atom and cerium atom. A strong main absorption edge with a high value of approximately $140\times10^4 cm^{-1}$ the deep ultraviolet region that is followed by secondary peaks at $35\times10^4 cm^{-1}$ in the 280 nm region show that the compounds demonstrate significant absorption at the ultraviolet region. At the same time, Mg_2CeO_4 (blue line) has a peak of $100\times10^4 cm^{-1}$ at the shortest wavelengths and a shoulder of $35\times10^4 cm^{-1}$ located at 320 nm. This high decrease in absorption with a decrease in wavelength towards the range of the visible spectrum indicates that the materials exhibit remarkable transparency to the emitted blue light [52]. The proportions of incident light reflected by the surface of the material are reflected in the reflectivity R(ω) spectrum, denoted by R [53]. Fig. 8(f) exhibits that the reflectivity is relatively low across the entire spectrum of light, which is beneficial at light-emitting applications because it allows high light to be transmitted or emitted instead of being reflected. The reflectivity peaks with values of about (25%) in the ultraviolet region and 0.17 in the 280 nm. In all three compounds, reflectivity is minimal (less than 0.12) in the visible range at wavelengths longer than 400 nm (which is one of the most important optical properties of these stacked perovskites). One of the crucial quantities that describes the collective oscillations of valence electrons, which are known as plasmons, is the electron energy loss function L(ω) [54]. Fig. 8(g) displays that the energy loss of all three materials is characterized by a series of sharp peaks in the UV region that represent the energy levels of the materials most prone to energy loss by electronic excitations. Ba_2CeO_4 (green line) has a strong energy loss peak at 280 nm, Sr_2CeO_4 (red line) at 220 nm and a secondary feature that is roughly at 260 nm, and Mg_2CeO_4 (blue line) has a broader peak This shifting of these peaks

to longer wavelengths as Mg is replaced by Ba means that the plasma frequency is reduced when the volume of the lattice of the layered perovskite is increased. Optical conductivity σ(ω) is a property that defines the conductivity of a material to electrical conductivity when it is exposed to the alternating electromagnetic field with the frequency [54]. The conductivity is greatest at the high-energy UV band, where photon energy is sufficient to excite electrons over the bandgap. In Ba_2CeO_4, there is a main peak of approximately 6500 ($Ohm^{-1}cm^{-1}$) in the deep ultraviolet region, with a secondary peak of 1500 ($Ohm^{-1}cm^{-1}$) at 280 nm. In Sr_2CeO_4, the primary peak is 6000 ($Ohm^{-1}cm^{-1}$) with a minor local High value of conductivity in the ultraviolet range, followed by a very strong decrease at visible ranges, confirm the idea that these materials are insulators in the visible spectrum but very active in the ultraviolet excitation, essential to their operation as blue phosphors.

Optical observation of Mg_2CeO_4, Sr_2CeO_4 and Ba_2CeO_4 on Fig.6(a-h) indicates that there is strong electromagnetic interaction in the UV and good transparency in the visible spectrum. Its real dielectric function, as well as its refractive index represent polarizability and ability to bend light, with the highest values of 5.0-5.2 and 2.2-2.4 respectively. The theoretical dielectric component, element, absorption coefficient as well as optical conductivity, suggest high UV absorptions, particularly in the Ba_2CeO_4, which is almost 6500 ($Ohm^{-1}Cm^{-1}$). The energy loss properties of the crystal lattice, the energy loss function (L) and the reflectivity (R), indicate that within the visual range, energy dissipation and surface reflections are minimal and light is able to propagate and escape the crystal lattice without interference [55]. Ruddlesden-Popper (RP) overlaid perovskites are optimum blue phosphors owing to the fact that the self-activated light of these phosphors is facilitated by a structural sandwich arrangement. Excitation energy is confined in the localized chain of octahedral chains of the material, CeO_6 [56], because of the one-dimensional RP phase traps (n=1) (graph e). This confined energy undergoes a charge transfer shift which produces blue-to Cynan light approximately at 470 nm. The high transparency of the materials in the visible domain prevents re-absorption and results in a high-intensity, efficient emission that is useful in advanced lighting systems.

3.4 Charge density and chemical bonding

Charge density (which is commonly denoted as the ρ(r) is the point of focus in the context of Density Functional Theory (DFT). Conventional quantum mechanics focuses on the complex

many-body wavefunction, but DFT makes the problem simpler by focusing on the spatial distribution of electrons [57].

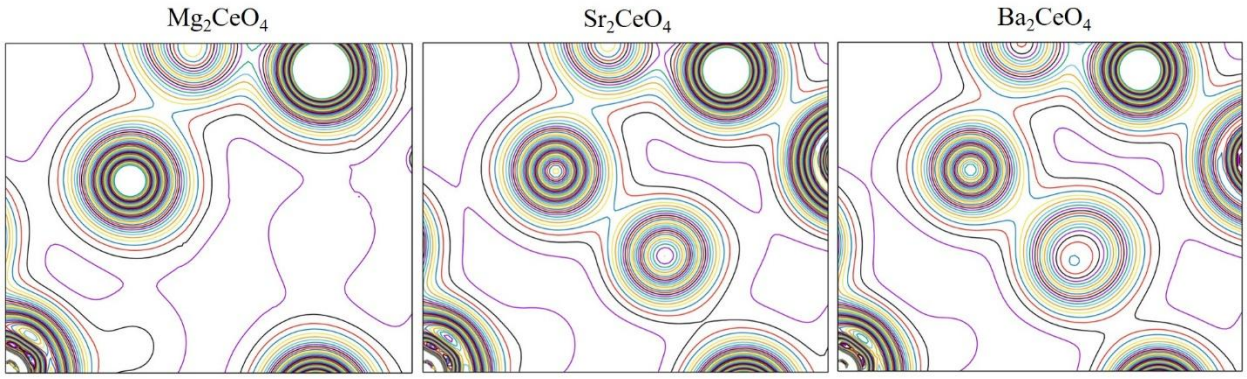


Fig 9. Electronic charge density of X_2CeO_4 (X = Mg, Sr, Ba)

The Fig.9 is a representation of the charge density $\rho(r)$ around the ions of Magnesium (Mg), Strontium, Barium and Cerium (Ce). The density appears in the form of clearly sharp concentric circles around the atoms. This is due to the fact that, cation and its charge to radius ratio is high, thus its electrons are strongly held. The resulting effect of this is that the electron cloud around magnesium is highly condensed. There are large white or low-density spaces between the atoms, which signifies not a lot of shares of electrons among Mg and O atoms. Instead, most of the electrons are bonded to the oxygen nuclei. It means that the affection within the material is mainly ionic. The charge density can be determined quantitatively as the sum of squares of the occupied Kohn Sham orbitals which can be written as:

$$\rho(r) = \sum |\psi i(r)|^2 \qquad (1)$$

The fact that there are no bridges between the lines of the contours means that there is no sharing of electrons by atoms. As a result, the electric attraction of the ions is the major force of bonding which is typical of ionic bonding [58]. The Fig.9 depicts the effect of the replacement of Magnesium by Strontium Sr. With a further movement along the periodic table, the atom of Sr_2CeO_4 has more electron shells, as it can be seen in the fact that the contour clusters are bigger in diameter. Being significant towards the neighboring Oxygen or Cerium atoms, the outside contour lines the valence regions show a slight extension. This indicates a shift where the bond is more ionic but also begins to be slightly covalent. The overlap of the electronic distributions of the cation and anion site is slightly higher in this case than in the combination of Mg. The change in

density distribution has a direct effect on the lattice constant and bulk modulus of the material due to the fact that the softer Sr ions under pressure, allow distinct electron interactions. The Barium ions, which carry the largest electronic footprint of the series in the concluding panel of Ba_2CeO_4 are the Barium ions. The contour lines are greatly more scattered and the same area bears most of the "necking" (to circles to oval or tear-drop shapes). In this picture it is shown that a compound is most polarizable and that is Ba_2CeO_4. There is an increase in the density of the interstitial areas and this suggests that the electrons are not localized to one nucleus as much as that of magnesium. This change can be considered using the Charge Density Difference equation: $\Delta\rho(r) = \rho_{bulk}(r) - \sum\rho_{atom}(r)$. All in this plot, the $\Delta\rho(r)$ implies that a lot of charge has been concentrated in the regions between the atoms of Barium and O, such that the Barium-O bond has a more complex electronic structure that can contribute to the unique luminous and dielectric properties are commonly seen in Barium-based cerates. Briefly, the charge density plots using DFT reveal that the reduction in the dominance of ionic bonding in Mg_2CeO_4 is replaced by increased polarizability and covalent nature in Ba_2CeO_4 with the increase in size of the cation. The distribution directly defines structural stability of the material and its electronic properties.

3.5 Phase stability and thermodynamic functions

Thermodynamics is the law that regulates the interaction of energy, temperature, work and heat in a system [59]. It explains the basic laws of energy transfer and conversion, why certain physical processes are spontaneous and some demand the input of some external energy. Thermodynamics assists scientists and engineers to anticipate matters with varying pressures and temperatures by relating the minute atomic movements to the macroscopic observations [60]. The Fig. 10(a) demonstrates the variation of G with temperature between 0 and 900 K. G refers to the chemical stability of a material phase at a specific temperature and pressure in thermodynamics. Non-linear Gibbs Free Energy of all three materials decreases with temperature. This decrease is attributed to the fact that the term of entropy (-TS) is more pertinent with increase in temperature. The molecule with the greatest or the lowest negative Gibbs Free Energy values in all temperatures is the molecule Mg_2CeO_4 (blue line).

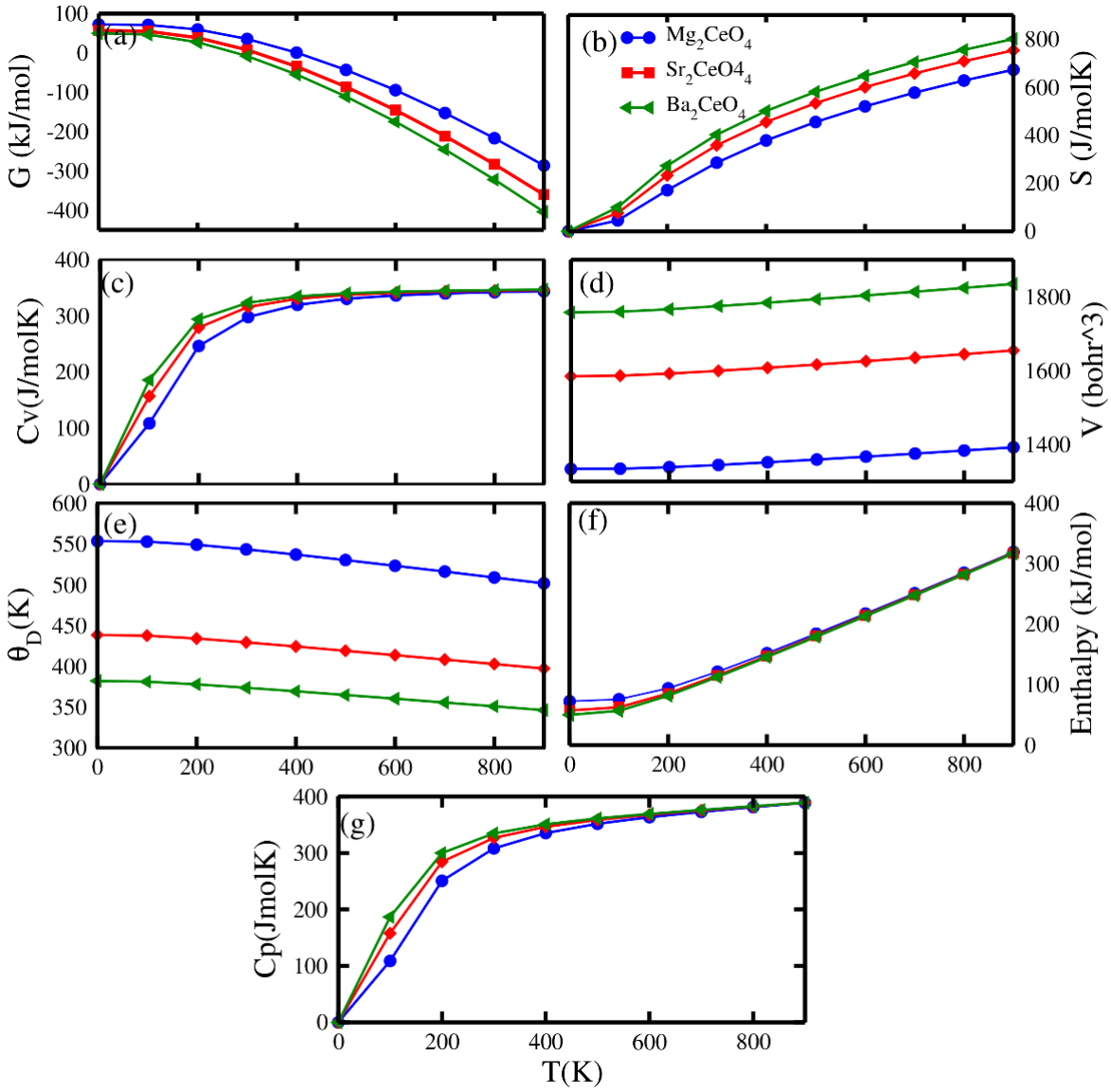


Fig 10. (a) Gibbs free energy, (b) Entropy, (c) Cv, (d) Volume, (e) Debye temperature, (f) Enthalpy, and (g) of X_2CeO_4 (X = Mg, Sr, Ba).

It begins at 60 kJ/mol at 0 K and decreases to -285 kJ/mol at 900 K. The Gibbs Free Energy values of the green line (Ba_2CeO_4) are the lowest. It starts with a value of approximately 50 kJ/mol in 0K, and decreases to -410 kJ/mol in 900K, the most negative value of all the materials. The barium-based compound gets more thermodynamically stable with increase in temperature compared to that at 0K. The Fig. 10(b) displays the entropy that is a measure of the thermal disturbance of the crystal lattice. The Third Law of Thermodynamics was that the entropy of all three compounds initially equals 0 J/mol K at absolute zero (0K). The increase in entropy is due to the activation of

phonon at a high temperature. The graphs indicate that the greater the alkaline earth metals, the greater the entropy at a particular temperature. The maximum value of entropy is 600 J/mol.K at 900 K, 750 J/mol.K at 900 K, and 820 J/mol.K at 900 K, respectively. Constant volume heat capacity which is represented as the Fig. 10(c) is used to determine the amount of heat mandatory to rise the temperature of a substance but the amount of space that the substance occupies does not change. Below the temperature ($T < 300$ K) the curves grow rapidly, and follows the T^3 law of power as one would expect in a solid-state material. When the temperature gets close to 900 K, curves are flattened and close to the classic Dulong-Petit limit. At low temperature, there are different tendencies of materials with the increase of Ba_2CeO_4 being the fastest. All the three curves converge as temperature increases. All the three materials reach plateau of about 345 J/mol.K at 900 K which means that the crystal lattice vibrational modes are practically fully stimulated. The Fig. 10(d) indicates the thermal expansion of the three materials. The higher the temperature, the stronger is the vibration of atoms, and the bigger is the unit cell volume (V) of 0 K to 900 K. The materials are arranged according to the size of alkaline earth cation (X = Mg, Sr, Ba). Mg_2CeO_4 (blue) possesses the least and smallest structure beginning at 1350 $bohr^3$ and rising up to about 1400 $bohr^3$. The middle one is Sr_2CeO_4 (red), with a diameter of approximately 1650 $bohr^3$. Ba_2CeO_4 (green) is the largest cation and its volume is the highest, which begins to be 1800 $bohr^3$ and increases to 1880 $bohr^3$ at 900 K. In Fig. 10(e) debye temperature is used to measure crystal lattice stiffness. Other properties, in contrast to Theta, Θ_D increases slightly with temperature because of lattice softening. The highest point of Debye temperature is 555 K at 0K and is reduced to 505K at 900K in Mg_2CeO_4 which shows highest interatomic bonding. Ba_2CeO_4, on the other hand, has the lowest Debye temperature and it begins at 385 K and lower to 350 K. The decreasing Θ_D constant of the barium compound corresponds to the increased entropy in Fig. 10(b), where the softer lattices allow the atoms to vibrate. The heat content or enthalpy of the system is indicated on Fig. 10(f). At 0 K, the internal energy of the crystal forms the base energy of all three materials. As the temperature increases, the enthalpy value increases gradually. The three materials have a similar pattern but deviate slightly at high temperatures. The highest enthalpy of all three compounds is obtained at 900 K at 330 kJ/mol. Such an upward trend is identical to the Gibbs Free Energy downward trend in Fig. 10(a), indicating absorption of thermal energy. Heat capacity at constant pressure (Cp) is similar to C_v (graph c), Cp increases strongly at low temperatures and then flattens. C_P is a little higher than C_V at high temperatures, since here C_P contains the thermal

expansion energy. At 900 K, all three materials attain a peak value of almost 390 J/mol/K. Owing to the green line (Ba_2CeO_4) being a bit higher at the low temperatures, it attains thermal saturation sooner than magnesium or strontium compounds. Thermodynamic examination of X_2CeO_4 (X = Mg, Sr, Ba) shows that when temperature exceeds 900 K, the materials would tend to expand in their volume and increase in the entropy, but the Gibbs Free Energy of the materials would decrease, indicating the improvement of thermal stability.

3.6 Thermoelectric transport coefficients

Advancement in this field heavily relies on the Density Functional Theory (DFT) combined with Boltzmann transport equations to predict electronic and vibrational properties [61]. With the calculation of the Seebeck coefficient, electrical conductivity, along with thermal conductivity, it is possible to identify high-performing materials to adopt waste heat recovery as well as solid-state cooling applications [62]. In Fig. 11(a-c) electrical conductivity of the relaxation time of X_2CeO_4 (X = Mg, Sr, Ba) yielded a significant impact on the material composition and chemical potential (Ef) with the peaks indicating areas of high carrier density relative to transport. After comparing the graphs, it can be seen that Mg_2CeO_4 has the smallest magnitude with its peak value of almost 10^{19}1/Ωms at Ef at approximately -2.0 Ry (a). On the other hand, the transport properties of Sr_2CeO_4 are much better, with the maximum of the same being approximately 7.0 $\times 10^{19}$ 1/Ωms at the same Fermi level (b). Finally, the significant difference between the peaks of Ba_2CeO_4 -6.5 $\times$ 10^{19} 1/Ωms at Ef = -2.0 Ry and all other three show uniformly low conductivity in the middle region around Ef = 0 Ry, thus confirming the semiconducting nature of these compounds, in which the band gap hinders movement of charge carriers. Fig. 11(d-f) show electronic thermal conductivity alienated by the relaxation time (κ_e/τ) of X_2CeO_4 (X = Mg, Sr, Ba), respectively. The following Fig. demonstrate heat flux due to charge carriers between chemical potentials of different values, and a direct correlation between the electrical conductivity distributions in the previous Fig. The conductivity in Mg_2CeO_4 (d) is quite modest, the highest value of about 0.3 $\times 10^{14}$ W/mKs at 200K just below Ef = -2.0 Ry. On the other hand, Sr_2CeO_4 (e) exhibits significantly better heat transmission with the highest heat transmission being at about 2.8 $\times 10^{14}$ W/mKs at the same level of energy. Finally, the maximum value of Ba_2CeO_4 (f) is approximately 0.3 $\times 10^{14}$ W/mKs at Ef -2.0 Ry. Values of all three materials consistently increase with temperature, which can be confirmed by the color, that is, green (200 K) to red (400 K) and purple (600 K),

decreasing to almost zero in the band gap region around Ef = 0 Ry, thus confirming the semiconducting nature in which the free carriers are absent and electronic thermal transport is heavily inhibited.

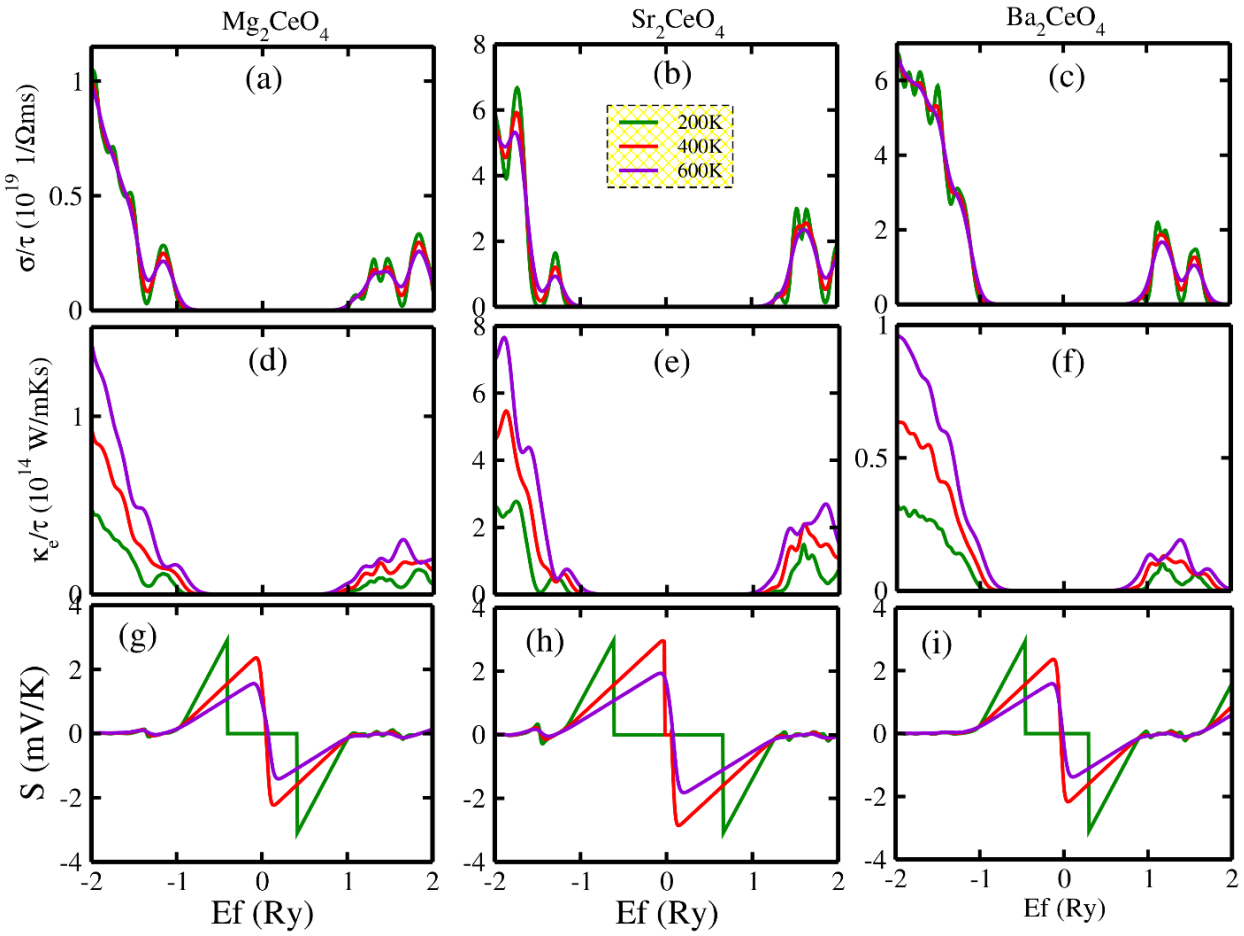


Fig 11. Calculated (a-c) electrical conductivity $\left(\frac{\sigma}{\tau}\right)$, (d-f) thermal conductivity, (g-i) Seebeck coefficients (S) of X_2CeO_4 (X = Mg, Sr, Ba).

The Seebeck coefficient (S) of X_2CeO_4 (X = Mg, Sr, Ba) in the existence of a temperature gradient in the crystal, indicative of the preponderant type of carrier, is shown in panels (g), (h) and (i). The observed two-polar signature in these plots is that as holes are the dominant carriers (negative Ef) and the reverse is also true (positive Ef). There is a sharp discontinuity across the band gap, where the material becomes more of a p-type rather than an n-type material. A peak value of 2.0 to 3.0 mV/K is attained by all three compounds with particular regard to lower temperatures (as indicated by the green line at 200K). Conversely, the elevated temperatures curves (red 400K and purple

600K) have smaller heights of the peaks and broadened profiles, which can be explained by the increased thermal activation of minorities that balance the Seebeck voltage. On comparison, it is observed that Mg_2CeO_4 and Ba_2CeO_4 have similar maxima magnitudes around 3.0 mV/K, whereas Sr_2CeO_4 has a slightly different profile, showing that again, the three have the same semi-conducting mechanism, but their respective band structure influences the precise magnitude and sensitivity of the thermoelectric response. Their unique electronic band structures determine the thermoelectric performance of X_2CeO_4 (X = Mg, Sr, Ba) in terms of their electronic conductivity, thermal conductivity along with the Seebeck coefficient. Both ratios, which are the ratios of σ/τ to κ_e/τ, show that there is sufficiently of carrier availability and thermal transport capacity above the band gap but the Seebeck coefficient is bipolar, which confirms that the material has semiconducting characteristics.

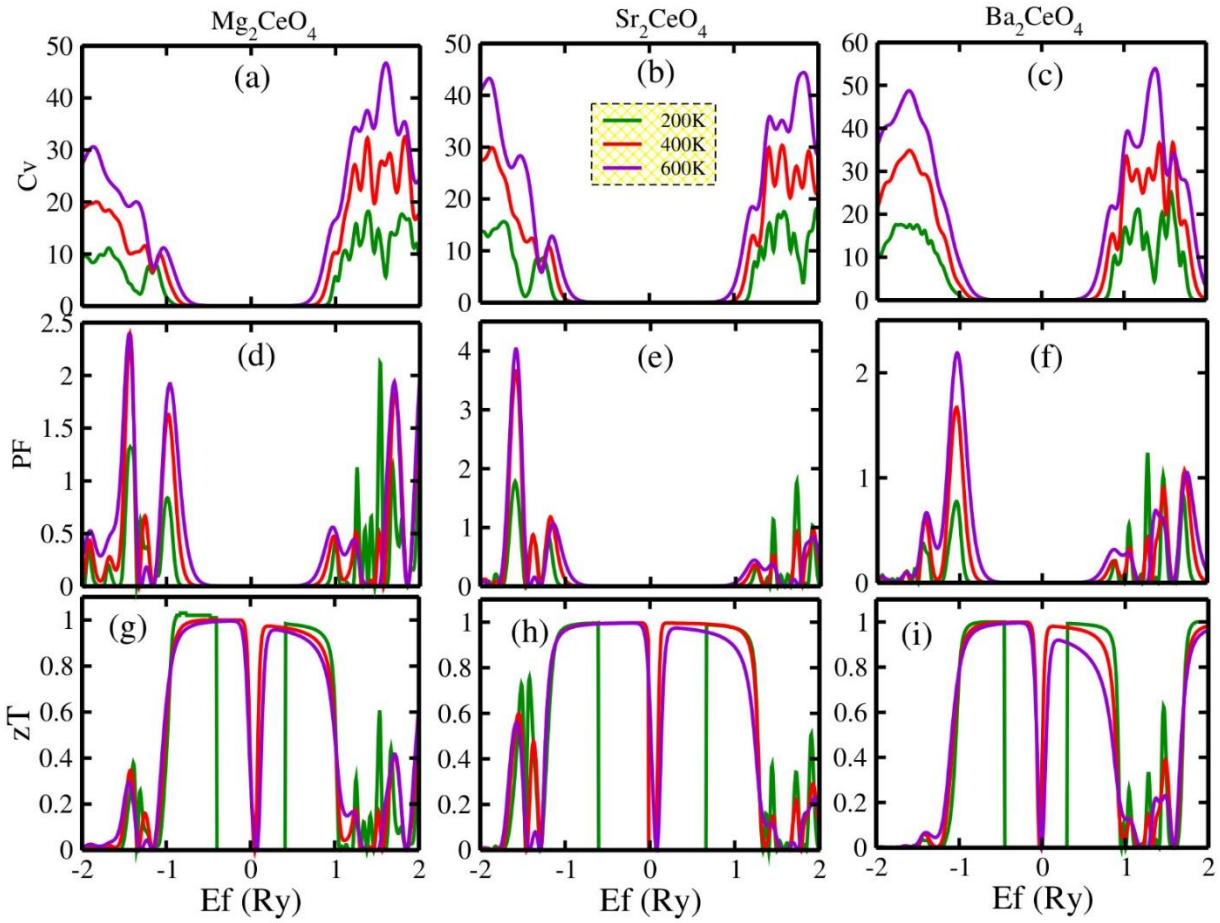


Fig. 12. Calculated (a-c) Cv, (d-f) PF (g-i) of X_2CeO_4 (X = Mg, Sr, Ba).

The specific heat at constant volume (Cv) is represented in the graph (a), (b), and (c) in fig 12. The three materials that were analyzed show that specific heat is directly proportional to temperature in all three instances. Those purple curves that represent 600 K always yield the best results followed by the red curves that represent 400 K, and the green curves that represent 200 K, which are at the bottom. Moreover, the three compounds have a distinct valley where Cv decreases to zero near the Fermi energy (E_f = 0 Ry), which is the energy gap of the materials, and in which case, there are no electronic states that can absorb thermal energy. Analyses of the exact values of the maximum temperature of 600 K allow a direct comparison of their capacities. In graph (a) of Mg_2CeO_4, the specific heat shows a peak near -30 on the negative side of the Fermi energy, with a maximum of about 47 near 1.6 Ry on the positive side. Graph (b) shows that Sr_2CeO_4 reaches strong peak of approximately 43 on the far negative axis at -2 Ry and a peak of approximately 45 on the positive axis. The Ba_2CeO_4 graph (c) is shifted up the y-axis to fit the higher values; the highest value is approximately 49 on the negative side and its maximum value is on the entire data set is approximately 54 at about 1.3 Ry.

Ba_2CeO_4 comes out as the most unchallenged leader in defining the best specific heat as the material with the highest capacity. It is always the highest overall in terms of value of Cv with the highest value of 54 at 600 K. This indicates that the compound containing Barium has a higher density of states to undergo thermal excitation compared to the magnesium and Strontium counterparts.

The calculated Power Factor (PF) of the 3 materials versus Fermi energy at different temperatures is plotted in graphs (d), (e), and (f). The power factor of graph (d) of Mg_2CeO_4 has a strong peak on the negative side of Fermi energy around -1.4 Ry, with a peak of about 2.4 at 600 K. A significant improvement in the negative axis can be observed in graph (e) of Sr_2CeO_4 with the peak value of the curve reaching almost 4 at 600 K, which is significantly different compared to both other compounds. The performance of Ba_2CeO_4 in graph (f) is more moderate, with the apex located on the negative axis towards -1.0 Ry and reaching a value of about 2.2 at 600 K. In the three materials, power factor generally increases with temperature, but there are large sharp spikes in the lowest temperature on the positive energy side (200 K). When comparing the three materials directly, Sr_2CeO_4 clearly shows higher values of power factor, reaching its highest 4.0, which is approximately twice that of the other two materials. The exceptionally high-power factor makes

the Strontium-based compound the most likely competitor of the three to work in practice as a thermoelectric power generator.

The three compounds are shown by their dimensionless figure of merit (zT), represented by graphs (g), (h), and (i) and this is the ultimate parameter of thermoelectric conversion efficiency in the three compounds. The zT value peaks with a value of 1.0 at graph (g) of Mg_2CeO_4 with vast plateaus between -1.0 and -0.4 Ry on the negative axis and between 0.2 and 0.9 Ry on the positive axis. In graph (h) of Sr_2CeO_4 the compound reaches a maximum zT value of 1.0, with an extremely wide negative plateau with a negative plateau value ranging between -1.1 and -0.1 Ry and a positive plateau value ranging between 0.1 and 1.1 Ry. Ba_2CeO_4 exhibits a peak zT of 1.0 in graph (i), with a steady plateau of about -1.0 to -0.1 Ry and another of 0.2 to 0.8 Ry on the positive axis. After evaluating the materials with the best zT values, all three are spectacular since they reach the highest theoretical limit of 1.0 in the assessments. However, Sr_2CeO_4 can be considered the best in general owing to the fact that it has much wider ranges of efficiencies than the other options. This wider plateau gives a more convenient energy range to chemical doping and Fermi level adjustment in the process of making thermoelectric devices.

4. Conclusions

This study gives a complete theoretical examination of the structural, mechanical, electrical, optical, thermodynamic, and plasmonic features of the Ruddlesden-Popper phase X_2CeO_4 (X = Mg, Sr, and Ba) compounds. The calculated electronic band structures show that these materials have direct band gaps ranging from 1.9 to 2.3 eV, classifying them as semiconductors and emphasizing their potential for solar applications. The optical properties, including optical conductivity, range from around 4500 to 6500 $Ohm^{-1}cm^{-1}$. The visible and near-ultraviolet bands have much higher dielectric constants (between 4 and 6), absorption coefficients (about 10^5 cm^{-1}), and refractive indexes (varying from 2 to 2.5), making them more useful in optoelectronic and photonic applications. Structural and mechanical stability suggests the applicability of compounds in flexible electronics. The thermodynamic analysis of X_2CeO_4 (X = Mg, Sr, Ba) shows that when the temperature exceeds 800 K, the materials expand in volume and entropy, while their Gibbs Free Energy drops, improving thermal stability. Moreover, the Mg_2CeO_4 exhibits a slightly higher zT (0.9) at ambient temperature. This study highlights the multifunctional features of layered

perovskites X_2CeO_4 and promotes their use in next-generation plasmonic as well as solar cell applications.

Acknowledgment

Princess Nourah bint Abdulrahman University Researchers Supporting Project number (PNURSP2026R70), Princess Nourah bint Abdulrahman University, Riyadh, Saudi Arabia

References

1. Wang, D., et al., *Early identification of breakthrough technologies: Insights from science-driven innovations.* Journal of Informetrics, 2025. **19**(1): p. 101606.
2. Mishra, P. and G. Singh, *Energy Management Systems in Sustainable Smart Cities Based on the Internet of Energy: A Technical Review.* Energies, 2023. **16**(19): p. 6903.
3. Sundaram, G.A. and G.r. Muniyandi, *Advancements in Renewable Energy: Innovations and Sustainable Solutions for a Greener Future.* Next Research, 2025. **2**(3): p. 100482.
4. Pioro, I.L., M.A. Makarem, and C.O. Zvorykin, *Wind-Energy Utilization and Sustainability*, in *Encyclopedia of Renewable Energy, Sustainability and the Environment (First Edition)*, M.R. Rahimpour, Editor. 2024, Elsevier: Oxford. p. 211-222.
5. Gebreabe, S.T., et al., *Advances in solar energy technologies: A comprehensive review of photovoltaic, thermal, and hybrid systems for sustainable energy solutions.* Next Research, 2026. **3**: p. 101176.
6. boutagount, S., et al., *Innovative materials for energy storage systems and photovoltaic solar technologies: A review.* Nano-Structures & Nano-Objects, 2025. **44**: p. 101562.
7. Khajuria, G., et al., *Photovoltaic–electrochemical coupled architectures for next-generation solar batteries.* Journal of Energy Storage, 2026. **154**: p. 121193.
8. Abraham, D.S., et al., *First-principles study of ZnO/MoSeTe van der Waals heterostructures for photovoltaic and hydrogen evolution applications.* RSC Advances, 2026. **16**(15): p. 13447-13453.
9. Achqraoui, M., et al., *Strain-driven optimization of bulk WSe2 for photovoltaic, photocatalytic, and thermoelectric applications: First-Principles insights.* International Journal of Hydrogen Energy, 2026. **222**: p. 154265.
10. Thakur, D.S., R.K. Sharma, and V. Garg, *Unveiling the photovoltaic potential of β-AgBiS2 for flexible solar cell applications: A DFT-Based investigation.* Materials Today Chemistry, 2026. **53**: p. 103488.
11. Mitrašinović, A.M., *Photovoltaics advancements for transition from renewable to clean energy.* Energy, 2021. **237**: p. 121510.
12. Younas, B., et al., *Mechanical, Optoelectronic, and Thermoelectric Performance of Li-based Double Perovskites Li2CuSbZ6 (Z = Cl, Br, I): First-Principles Calculations.* Journal of Inorganic and Organometallic Polymers and Materials, 2024. **34**(10): p. 4828-4841.
13. Ziar, H., et al., *Photovoltatronics: intelligent PV-based devices for energy and information applications.* Energy & Environmental Science, 2021. **14**(1): p. 106-126.
14. Sayed, E.T., et al., *A critical review on environmental impacts of renewable energy systems and mitigation strategies: Wind, hydro, biomass and geothermal.* Science of The Total Environment, 2021. **766**: p. 144505.
15. Briceño, G., et al., *A Class of Cobalt Oxide Magnetoresistance Materials Discovered with Combinatorial Synthesis.* Science, 1995. **270**(5234): p. 273-275.
16. Danielson, E., et al., *A rare-earth phosphor containing one-dimensional chains identified through combinatorial methods.* Science, 1998. **279**(5352): p. 837-9.
17. Hirai, T. and Y. Kawamura, *Preparation of Sr2CeO4 Blue Phosphor Particles and Rare Earth (Eu, Ho, Tm, or Er)-Doped Sr2CeO4 Phosphor Particles, Using an Emulsion Liquid Membrane System.* The Journal of Physical Chemistry B, 2004. **108**(34): p. 12763-12769.

18. Atchyutha Rao, C., P. Rao V. Nannapaneni, and K. V. R. Murthy, *Characterization and Photoluminescence Of Sr2CeO4: Eu+3, La+3.* Advanced Materials Letters, 2013. **4**(3): p. 207-212.
19. Polman, A., et al., *Photovoltaic materials: Present efficiencies and future challenges.* Science, 2016. **352**(6283): p. aad4424.
20. Schlipf, J.B., *Enhancement of group-IV optoelectronic sensing devices through materials engineering and nanostructuring*

Verbesserung von optoelektronischen Sensoren der Gruppe IV durch Werkstofftechnik und Nanostrukturierung. 2024.
21. Talik, E., et al., *Electronic structure analysis and properties of Sr2CeO4 grown by sol–gel method.* Materials Research Bulletin, 2012. **47**(11): p. 3107-3113.
22. Stefanski, M., et al., *Influence of grain size on optical properties of Sr2CeO4 nanocrystals.* J Chem Phys, 2015. **142**(18): p. 184701.
23. Blaha, P., et al., *WIEN2k: An Augmented Plane Wave plus Local Orbitals Program for Calculating Crystal Properties.* Technische Universität Wien, Wien, 2001. **28**.
24. Blaha, P., et al., *Full-potential, linearized augmented plane wave programs for crystalline systems.* Computer Physics Communications, 1990. **59**(2): p. 399-415.
25. Koller, D., F. Tran, and P. Blaha, *Improving the modified Becke-Johnson exchange potential.* Physical Review B, 2012. **85**(15): p. 155109.
26. Bandhaso, D., A. Lukmantoro, and S. Sholihun, *COMPARATIVE STUDY OF EOS (EQUATION OF STATES) MODELS FOR FITTING ENERGY VERSUS VOLUME DATA IN THERMODYNAMICS.* JOURNAL ONLINE OF PHYSICS, 2024. **9**(2): p. 102-106.
27. Waheed, H.S., et al., *Enhanced Device Absorption Efficiency and Photocatalytic Response of Monolayer PtX2 (X = S, Se, Te) for Photocatalysis and Solar Cell Applications.* physica status solidi (b), 2023. **260**(7): p. 2300028.
28. Yasir, M.A., et al., *A First-Principles Insight to Explore the Optoelectronic, Thermodynamic, and Transport Properties of Ferromagnetic Double Perovskites Li_2CuOsX_6 (X = Cl, Br) for Energy Conversion Applications.* Journal of Inorganic and Organometallic Polymers and Materials, 2026. **36**(1): p. 279-298.
29. Ullah, H., et al., *Influences of vacancy and doping on electronic and magnetic properties of monolayer SnS.* Journal of Applied Physics, 2018. **124**(6).
30. Waheed, H.S., et al., *Optoelectronic and photocatalytic properties of Mo-based Janus monolayers for solar cell applications.* Optik, 2022. **271**: p. 170071.
31. Yousuf, M., et al., *A computational insight of the physical properties of MoSX (X= Cl, Br, I) for green energy applications.* RSC Advances, 2025. **15**(55): p. 47282-47290.
32. Brik, M.G., A. Suchocki, and A. Kamińska, *Lattice Parameters and Stability of the Spinel Compounds in Relation to the Ionic Radii and Electronegativities of Constituting Chemical Elements.* Inorganic Chemistry, 2014. **53**(10): p. 5088-5099.
33. Abbas, Y.M. and Y.R. Alharbi, *Multiple-criteria optimization of ternary-cementitious concrete formulations: An evolutionary data-driven framework for high-performance, cost-efficiency, and sustainable designs.* Structures, 2025. **80**: p. 109955.

34. Hussain, A., et al., *Theoretically explore XRD analysis and multi-functional properties of Ruddlesden popper phase family member Sr2XO4 (X = Ce, Hf, Ti and Zr) for photovoltaic applications.* Chemical Physics, 2025. **598**: p. 112834.
35. Verma, H., A. Tripathi, and S. Upadhyay, *Investigation of structural, optical, dielectric properties, and electrical conductivity mechanism of Sr2CeO4: Experimental and DFT studies.* Materials Science in Semiconductor Processing, 2025. **189**: p. 109309.
36. Yasir, M.A., et al., *Halide-driven band engineering in double perovskites Cs2LiIrX6 (X = Cl/ Br) for photovoltaic and thermoelectric applications; DFT study.* Journal of Molecular Graphics and Modelling, 2026. **148**: p. 109528.
37. Ahsan, M., et al., *A first-principles study on the structural, optoelectronic, thermoelectric, elastic and thermodynamic functionality of lead-free direct bandgap double perovskites Rb2LiIrX6 (X = Cl/Br).* Modern Physics Letters B. **0**(ja): p. null.
38. Ali, F., et al., *Optoelectronic and thermoelectric response of lead-free halide double perovskites Rb2BiAuX6 (X = Cl, Br, I) for energy storage applications.* RSC Advances, 2025. **15**(45): p. 37999-38013.
39. Wang, W., et al., *The size effect to O2- -Ce4+ charge transfer emission and band gap structure of Sr2 CeO4.* Luminescence : the journal of biological and chemical luminescence, 2018. **33 5**: p. 907-912.
40. Eibert, M., et al., *Effects of chemical disorder and spin-orbit coupling on the electronic-structure and Fermi-surface topology of YbSb-based monopnictides.* Physical Review B, 2025. **112**(3): p. 035106.
41. Dhar, S., *Basics of Crystal Structure, Band Structure and Lattice Vibrations in Solids*, in *Excitons in Semiconductors*, S. Dhar, Editor. 2025, Springer Nature Switzerland: Cham. p. 1-25.
42. Du, Y., et al., *Strain-tuning the optoelectronic and mechanical properties of Cs_2AgSbX_6 (X = Cl, Br, I): A combined computational study of electronic structure and property underpinnings.* Computational and Theoretical Chemistry, 2026. **1257**: p. 115658.
43. Parajuli, S., M. Irfan, and M. Akyol, *Structural, magnetic and optical characterization of BiFe1-xCrxO3 (x = 0.0, 3.3, 6.6 and 10 %) nanoparticles.* Next Materials, 2026.
44. Fan, D., et al., *The transition from indirect band gap to direct band gap and effectively separating of electron-hole pairs in h-BC2N/MoSi2N4 heterojunction for photocatalytic water splitting.* International Journal of Hydrogen Energy, 2025. **107**: p. 452-459.
45. *Appendices*, in *Density-Of-States Function and Related Applications in Quantized Structures*. p. 991-1019.
46. Mengesha, W.G. and K. Nagessar, *Advanced thermal and magnetic materials for high-power and high-temperature applications: a comprehensive review.* Discover Materials, 2025. **5**(1): p. 180.
47. Hussain, A., et al., *Theoretical investigation of Ruddlesden Popper phase La2XO4(X = Zn, Ca, Mg, and Be) compounds with multifunctional properties for flexible photovoltaic applications.* Journal of Electroceramics, 2025. **53**(3): p. 321-334.
48. Jawad, M., et al., *K2AlAgCl6: A new stable and eco-friendly double perovskite candidate for UV optoelectronic and thermoelectric devices.* Chemical Physics, 2026. **604**: p. 113094.
49. Boudebs, G., et al., *Simplified Kerr refractive index measurement in the visible range using phase object contrast imaging.* Optics & Laser Technology, 2026. **198**: p. 114888.

50. Jubu, P.R., et al., *Accuracy in estimating the absorption coefficient of powdered nanomaterials: resolving misconceptions in tauc plot application for energy bandgap determination.* Journal of Materials Science: Materials in Electronics, 2025. **36**(16): p. 961.
51. Jabeen, N., et al., *A DFT analysis on the electronic, mechanical, optical, elastic, structural and thermodynamic properties of XBiNb2O7 (X = Cs, Rb, K and Na) for photovoltaic applications.* Computational Condensed Matter, 2025. **44**: p. e01063.
52. Abd El-kawy, F.S., et al., *Effective UV and blue light blocking filters with high visible transparency utilizing graphene quantum dots.* Dyes and Pigments, 2025. **239**: p. 112802.
53. Li, H., et al., *Investigation on Mixed Reflection Behavior of Cool Pavement Coating and Its Impact on Safety of Road Light Environment.* Engineering, 2025.
54. Lebedev, V. and A. Kondorskiy, *Optics of plasmon-exciton nanostructures: theoretical models and physical phenomena in metal/J-aggregate systems.* Uspekhi Fizicheskih Nauk, 2024. **195**.
55. Nipun, M.K., et al., *Broadband solar energy harvesting with a machine-learning-optimized nickel–quartz metamaterial absorber.* Journal of Nanophotonics, 2025.
56. Zhang, Y., et al., *Unraveling the physical chemistry and materials science of CeO2-based nanostructures.* Chem, 2021. **7**(8): p. 2022-2059.
57. Schuch, N. and F. Verstraete, *Computational complexity of interacting electrons and fundamental limitations of density functional theory.* Nature Physics, 2009. **5**(10): p. 732-735.
58. Marje, S.J., et al., *Progress and prospects of Ni–Co layered double hydroxides for advanced energy storage in rechargeable supercapacitors and batteries.* Progress in Materials Science, 2026: p. 101702.
59. Ragab Mahmoud, A., *First Law of Thermodynamics: Energy Conservation in Heat and Work*. 2025.
60. de Hemptinne, J.-C., et al., *A View on the Future of Applied Thermodynamics.* Industrial & Engineering Chemistry Research, 2022. **61**(39): p. 14664-14680.
61. Latif, A., et al., *Density functional theory for nanomaterials: structural and spectroscopic applications—a review.* Journal of Molecular Modeling, 2025. **31**(8): p. 211.
62. Shi, X.L., et al., *Toward Efficient Thermoelectric Materials and Devices: Advances, Challenges, and Opportunities.* Chem Rev, 2025. **125**(16): p. 7525-7724.